PHYSICAL REVIEW B **101**, 064405 (2020)

Magnetic and transport properties of the pyrochlore iridates $(Y_{1-x}Pr_x)_2Ir_2O_7$: Role of f-d exchange interaction and d-p orbital hybridization

Harish Kumar,[1] K. C. Kharkwal,[1] Kranti Kumar,[2] K. Asokan,[3] A. Banerjee,[2] and A. K. Pramanik[1,*]

[1]*School of Physical Sciences, Jawaharlal Nehru University, New Delhi 110067, India*
[2]*UGC-DAE Consortium for Scientific Research, Indore 452001, India*
[3]*Materials Science Division, Inter University Accelerator Centre, New Delhi 110067, India*

(Received 15 October 2019; revised manuscript received 7 December 2019; accepted 13 January 2020; published 5 February 2020)

The f-d magnetic exchange interaction is considered to be a key ingredient for many exotic topological phases in pyrochlore iridates. Here, we have investigated the evolution of structural, magnetic, and electronic properties in doped pyrochlore iridate, $(Y_{1-x}Pr_x)_2Ir_2O_7$. Apart from geometrical frustration, pyrochlore iridates are well known for their active spin-orbit-coupling effect. The substitution of Pr^{3+} $(4f^2)$ for the nonmagnetic Y^{3+} $(4d^0)$ acts as a magnetic doping, which provides an ideal platform to study f-d exchange interaction without altering the Ir sublattice. With Pr substitution, the system retains its original cubic structural symmetry, but the local structural parameters show an evolution with the doping concentration x. The robust magnetic-insulating state in $Y_2Ir_2O_7$ is drastically weakened, while $Pr_2Ir_2O_7$ $(x = 1.0)$ shows a paramagnetic-metallic behavior. A metal-insulator transition is observed for the $x = 0.8$ sample. This evolution of magnetic and electronic properties is believed to be induced by an exchange interaction between localized Pr-$4f$ and itinerant Ir-$5d$ electrons, as well as by an increased hybridization between Ir-t_{2g} and (basal) O-p orbitals, as observed in x-ray absorption spectroscopy study. The resistivity in insulating materials follows a power-law behavior with a decreasing exponent with x. A negative magnetoresistance is observed for the present series of samples at low temperature and where the magnetoresistance shows a quadratic field dependence at higher fields.

DOI: 10.1103/PhysRevB.101.064405

I. INTRODUCTION

Geometrical frustration is inherent to pyrochlore systems, which provides many interesting properties [1–6]. The frustration mainly arises due to interpenetrating tetrahedra, where the magnetic ions sitting at the vertices of the tetrahedra introduce magnetic frustration for antiferromagnetic (AFM) interactions. Ir-based pyrochlores ($A_2Ir_2O_7$, where A is the trivalent rare-earth element) have recently drawn significant interest due to their novel topological phases of matter [7–9]. Apart from geometrical frustration, pyrochlore iridates share a comparable energy scale between spin-orbit coupling (SOC), electronic correlation (U), and crystal-field effect (CFE) due to $5d$-based heavy Ir atoms ($Z = 77$). This complex interplay between these energies is believed to be a key ingredient for many interesting properties in this class of materials.

The size of A-site cations has an important role in the physical properties of pyrochlore iridates, giving rise to magnetic insulating to nonmagnetic complex metallic phases with increasing ionic radii [10]. The magnetic nature of A ions further introduces complication to the magnetic behavior due to the possibility of f-d exchange interactions between Ir and A ions [11]. $Y_2Ir_2O_7$ is an important member of the pyrochlore iridate family which has nonmagnetic Y^{3+} at the A site, and shows an insulating behavior and an AFM-type magnetic transition with ordering temperature $T_N \sim 160$ K [12–22]. Given magnetically inactive Y^{3+}, this magnetic ordering is only associated with the Ir sublattice. The low-temperature magnetic state in $Y_2Ir_2O_7$ has been investigated using different microscopic tools. For instance, muon spin relaxation (μSR) measurements have shown spontaneous oscillation in muon symmetry, indicating a magnetically long-range ordering at low temperature [12,23]. The neutron powder diffraction (NPD) measurements, on the other hand, have not ruled out the possibility of long-range magnetic ordering, but because iridium is a strong absorber of neutrons, the NPD measurements remain largely insensitive for Ir-containing materials [13]. Recently, using magnetic relaxation measurements, we have shown a nonequilibrium magnetic ground state in $Y_2Ir_2O_7$ and its doped samples [18–20]. Theoretically, this material is described as a possible candidate of a Weyl-type semimetal with a noncoplanar AFM structure [24]. The $Pr_2Ir_2O_7$, on the other hand, is another interesting compound in pyrochlore iridates which has a magnetic and comparatively large A-site ion, Pr^{3+} $(4f^2)$. In another sense, this material has two active (Pr and Ir) sublattices. This material is metal and shows a nonmagnetic character, even though an AFM-type Ruderman-Kittel-Kasuya-Yosida (RKKY) interaction with energy scale $|T^*| = 20$ K between Pr-$4f$ moments has been observed, which is mediated through Ir-$5d$ delocalized electrons [4,25]. The AFM interaction is suppressed due to the screening of $4f$ moments through the Kondo effect, which decreases the Weiss temperature down to $\theta_P = 1.7$ K. $Pr_2Ir_2O_7$ is shown to exhibit spin-liquid behavior where the system does not show any trace of magnetic ordering, even down to 70 mK [4]. Instead, a

---

[*] akpramanik@mail.jnu.ac.in

partial spin freezing of Pr-4f moments is observed at 120 mK [4]. A large value of the calculated frustration parameter ($f = 70$) indicates high frustration in this material. Further, an unconventional anomalous Hall effect has been observed below 1 K in $Pr_2Ir_2O_7$, which is explained with the spin-chirality effect in Ir-5d electrons due to the noncoplanar spin structure of Pr spins [26].

In the present study, we have attempted to understand the evolution of magnetic and transport properties in pyrochlore iridate $(Y_{1-x}Pr_x)_2Ir_2O_7$ where Y^{3+} is progressively replaced with Pr^{3+}. This substitution induces f-d interaction between Pr-4f and Ir-5d localized spins, but other basic interactions such as SOC and U remain largely unaffected. The f-d exchange interaction along with the correlation effect have been theoretically shown to induce exotic topological electronic phases in pyrochlore iridates [11]. However, since Pr^{3+} is a large ion, it is likely to induce local structural modification, which as a result will influence the Ir-O interactions and hybridization. It is very important to investigate the evolution of the magnetic and transport properties in the present series, as $Y_2Ir_2O_7$ shows a high ordering temperature ($T_N \sim 160$ K) with a nonmagnetic A-site atom, whereas $Pr_2Ir_2O_7$ avoids long-range magnetic ordering in spite of having a magnetic ion sitting at the A site. This draws further attention as recently a new type of quantum criticality, based on an interplay between SOC and U, has been proposed in pyrochlore iridates with a model system of $(Y_{1-x}Pr_x)_2Ir_2O_7$ [27].

Our results show that the original cubic structural symmetry is retained in the $(Y_{1-x}Pr_x)_2Ir_2O_7$ series, but a minor modification in the structural parameters is observed. The magnetic ordering temperature progressively decreases with Pr substitution, where $Pr_2Ir_2O_7$ shows complete paramagnetic (PM) behavior. Similarly, this system shows a progressive metallic behavior exhibiting a metal-to-insulator transition for $x = 0.8$ samples, where an enhanced Ir-O hybridization with an increasing Pr concentration plays a crucial role.

II. EXPERIMENTAL DETAILS

A series of polycrystalline samples of $(Y_{1-x}Pr_x)_2Ir_2O_7$, with $x = 0.0$, 0.05, 0.1, 0.2, 0.4, 0.6, 0.8, and 1.0, have been prepared using the standard solid-state route [18–21]. Powder material ingredients Y_2O_3, Pr_6O_{11}, and IrO_2 with a phase purity of more than 99.99% (M/s Sigma-Aldrich) are mixed in stoichiometric ratio and ground well. The powder materials Y_2O_3 and Pr_6O_{11} have been given a preheat treatment at 800° C for around 8 hours to remove any residual atmospheric moisture. The well-ground mixture is subsequently pelletized and sintered in air at a temperature range between 1000° and 1160° C for about 19 days, with several intermediate grindings. The crystal structure and phase purity of these materials have been checked with powder x-ray diffraction (XRD) using a Rigaku diffractometer attached with CuK_α radiation. XRD data are collected in the range of $2\theta = 10 - 90^\circ$ at a step of $\Delta 2\theta = 0.02^\circ$. The XRD data have been analyzed using the Reitveld refinement program FULLPROF by Rodriguez-Carvajal [28]. X-ray absorption measurements were performed at beam lines of 20A1 HSGM and 17C1 Wiggler of NSRRC, Taiwan as per standard procedure and data analysis. DC magnetization (M) measurements have been carried out with a superconducting quantum interference device (SQUID, Quantum Design) magnetometer. Electrical transport properties have been measured using an integrated system from NanoMagnetics Instruments and Cryomagnetics, Inc.

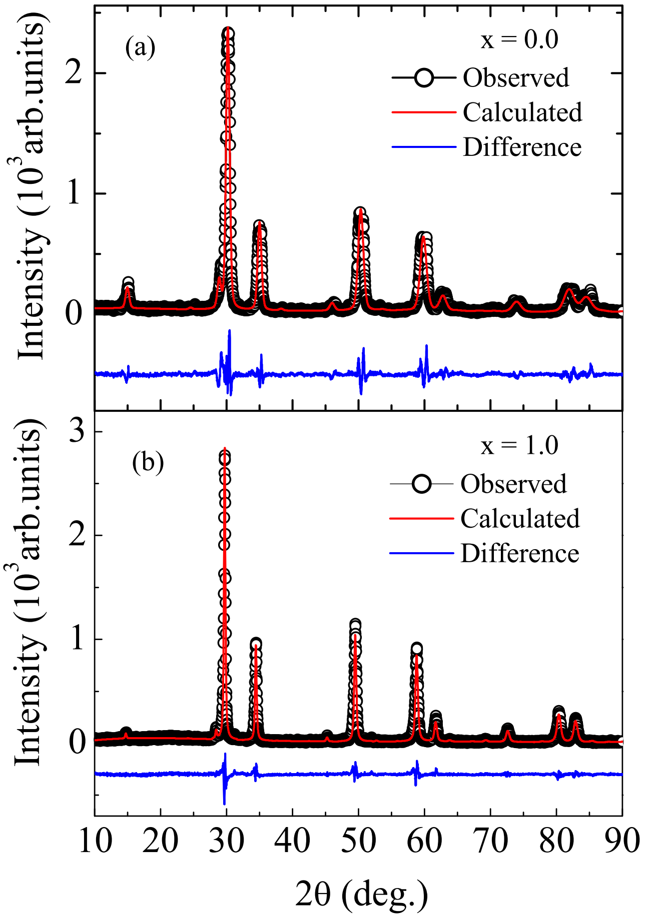

FIG. 1. Room-temperature XRD pattern along with Rietveld analysis for the $(Y_{1-x}Pr_x)_2Ir_2O_7$ series with (a) $x = 0.0$ and (b) $x = 1.0$.

III. RESULTS AND DISCUSSIONS

A. Structural analysis

The XRD pattern along with Rietveld refinement are shown for two end members of the series, i.e., $Y_2Ir_2O_7$ and $Pr_2Ir_2O_7$, in Figs. 1(a) and 1(b), respectively. The XRD data for $x = 0.0$ in Fig. 1(a) are, in fact, shown in our previous reports [18,19], and are shown again here for comparison in the present series. With Pr substitution, no significant modification is observed in the XRD pattern in terms of peak position or the arising of new peak(s). The Rietveld refinement of the XRD data for $Y_2Ir_2O_7$ and the whole series shows that the materials crystallize in cubic $Fd\bar{3}m$ symmetry. We obtain a reasonably good fitting of Rietveld refinement, obtaining goodness of fit (GOF $= R_{wp}/R_{\mathrm{exp}}$) values of the fitting between 1.5–2.0. We find no structural phase transition with Pr substitution; however, the structural parameters show an evolution with doping x, as shown in Fig. 2. Considering a slight mismatch in the ionic radii between Y^{3+} (1.019 Å)

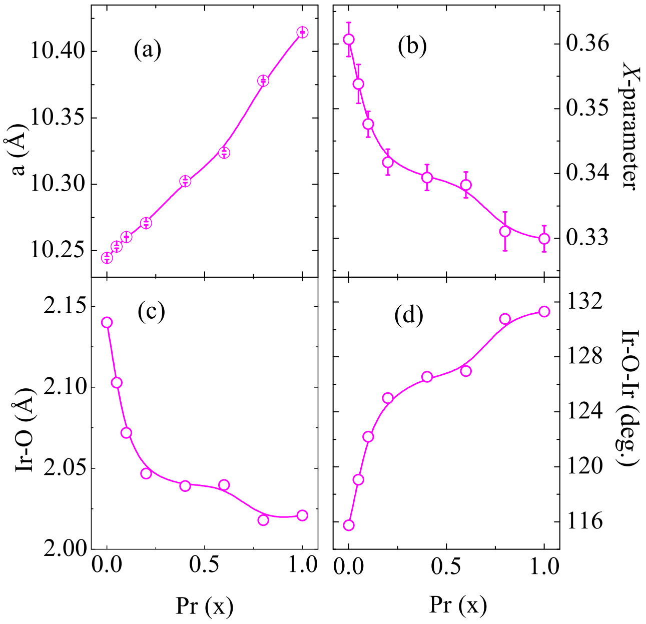

FIG. 2. (a) Lattice constant a, (b) X parameter of O atom, (c) Ir-O bond length, and (d) Ir-O-Ir bond angle as a function of Pr substitution for the $(Y_{1-x}Pr_x)_2Ir_2O_7$ series. Lines are a guide for the eyes.

and Pr^{3+} (1.126 Å), changes in the structural parameters are expected. The unit-cell parameter (a) for the parent compound $Y_2Ir_2O_7$ is found to be $a = 10.244(1)$ Å, which increases almost linearly with a slope of about 0.17 upon substitution of Pr. For $Pr_2Ir_2O_7$ ($x = 1$), a is found to be 10.4145 Å [Fig. 2(a)] and the change in a mostly follows Vegerd's law. The XRD pattern as well as the lattice parameter for both $Y_2Ir_2O_7$ and $Pr_2Ir_2O_7$ match well with the previous reports [12,13,16,18,19,29,30]. The change in a is about 1.6% over the whole series, which can be explained due to the larger ionic size of Pr^{3+} compared to Y^{3+} ions. Here, we add that the structural parameters in the present series are obtained from Rietveld analysis of the XRD data, which is basically a bulk measurement and remains largely insensitive to local variation. We find that all of the samples are "uniform" in terms of chemical phase purity, where the Rietveld analysis implies an absence of any unwanted chemically impure phase. Given that Y^{3+} and Pr^{3+} have a difference in ionic radii and randomly populate the A site, there would be a local disorder which cannot be understood from the XRD data.

In the pyrochlore structure, there are mainly two variable X parameters such as the lattice constant (a) and the parameter associated with the oxygen position. This X parameter plays a significant role in determining the electronic and magnetic properties in this class of materials [7]. For instance, it decides the structural organization of the IrO_6 octahedra, which is crucial in pyrochlore systems to decide its structural stability and physical properties. Figure 2(b) presents an evolution of the X parameter with Pr concentration. In general, sixfold coordinated Ir ions in IrO_6 octahedra have an equal Ir-O bond length (d_{Ir-O}). The X parameter for an undistorted IrO_6 octahedron turns out to be $X_{\text{ideal}} = 0.3125$, which generates a perfect local cubic crystal field. The deviation of X from its ideal value generates a trigonal crystal field, which modifies the orbital ordering or local hybridization [31,32]. The X value (0.36) for $Y_2Ir_2O_7$ implies that the IrO_6 octahedra are distorted, which lowers the symmetry by compressing the octahedra. Figure 2(b) depicts that the X parameter decreases over the series, which is suggestive of decreasing trigonal distortion with Pr. This variation of the X parameter is, however, directly associated with the $\langle$Ir-O-Ir$\rangle$ bond angle and the Ir-O bond length, and hence hopping of charge carriers. Figures 2(c) and 2(d) show the change of Ir-O bond length and $\langle$Ir-O-Ir$\rangle$ bond angle, respectively with Pr doping. The Ir-O bond length decreases while the $\langle$Ir-O-Ir$\rangle$ bond angle increases with x. This implies that with Pr doping, the distortion in the IrO_6 octahedra decreases and the Ir-$5d$/O-$2p$/Ir-$5d$ orbital overlapping increases, which would facilitate the hopping of itinerant Ir-$5d$ electrons.

B. X-ray absorption spectroscopy study

The x-ray absorption spectroscopy (XAS) measurements have been done on selected samples ($x = 0.0$, 0.4, and 1.0) of the present series to understand the cationic charge state and the Ir-O hybridization state. The L_2 ($2P_{1/2} \rightarrow 5d$) and L_3 ($2P_{3/2} \rightarrow 5d$) absorption edge for the Ir^{4+} ($5d^5$) electronic state in XAS occurs at 12.824 and 11.220 keV of energy, respectively [33,34]. While the L_2 edge is mainly related to transitions of the $5d_{3/2}$ holes, the L_3 absorption edge involves the transition of both $5d_{3/2}$ and $5d_{5/2}$ states [34,35]. Therefore, the relative intensity of the L_2 and L_3 edges (the so-called statistical branching ratio) gives information about the ground-state expectational value of the SOC $\langle \mathbf{L} \cdot \mathbf{S} \rangle$ of the $5d$ states. In the present series, the SOC effect is unlikely to change, and hence we have focused only on the L_3 absorption edge spectra.

Figure 3(a) shows the normalized XAS spectra collected at the L_3 absorption edge for the present series (the data for $x = 0.4$ and 1.0 are shifted vertically). As evident in Fig. 3(a), the L_3 edge occurs at 11.220 keV, which is in agreement with other Ir-based materials (i.e., Na_2IrO_3, Sr_2IrO_4, and $Y_2Ir_2O_7$) [33–35]. We find that the position of the L_3 edge shifts toward lower energy with progressive substitution of Pr (i.e., 11220.24, 11219.99, and 11219.91 eV for $x = 0.0$, 0.4, and 1.0, respectively). The change in the L_3 peak position is small ($\Delta E \sim -0.33$ eV) over the series, where the left inset of Fig. 3(a) shows a magnified view of the absorption peak. We understand that this change in the L_3 peak position is due to the change in the Ir charge state ratio. Our recent x-ray photoemission spectroscopy (XPS) study shows that Ir^{4+} is a major component, while a small amount (~5.4%) of coexisting Ir^{5+} ions has been observed in $Y_2Ir_2O_7$ [19]. The small shifting of the L_3 peak toward lower energy is possibly due to the removal of Ir^{5+} ions with Pr substitution. To further understand this, we have plotted the second derivative of the L_3 spectra in the right inset of Fig. 3(a). As evident in this figure, the derivative shows a shoulder on both sides of the main peak for $x = 0.0$, while this shoulder disappears for the doped materials ($x = 0.4$ and 1.0). The shoulder in the second derivative is considered to be an indication of coexisting Ir^{5+} ions, which disappears with Pr substitution [36].

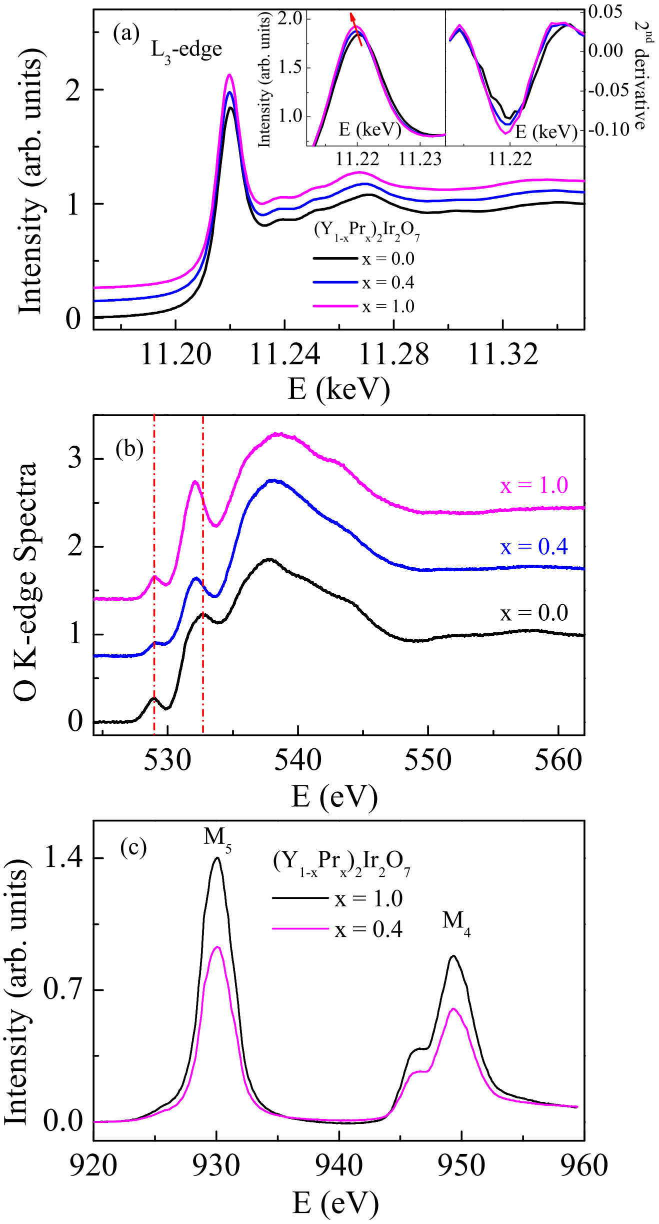

FIG. 3. (a) XAS spectra at the L_3 edge for the $(Y_{1-x}Pr_x)_2Ir_2O_7$ series with $x = 0.0$, 0.4, and 1.0. XAS data for $x = 0.4$ and 1.0 are shifted vertically for clarity. The left and right insets show a magnified picture of the L_3 absorption edge across 11 220 eV and a second derivative of peaks, respectively. (b) Low-energy O K-edge XAS spectra for the same $x = 0.0$, 0.4, and 1.0 materials. (c) Normalized M_4 and M_5-edge XAS spectra as a function of energy for $x = 1.0$ and 0.4.

Further, to understand the unoccupied Ir-d states or hybridization between the Ir-d and O-$2p$ states, we have carried out XAS measured at the O-K edge at room temperature. Due to the crystal-field effect, Ir-d orbitals are split into low-lying t_{2g} (d_{xy}, d_{xz}, and d_{yz}) and e_g ($d_{x^2-y^2}$ and d_{z^2}) states, where a strong SOC further splits the t_{2g} state into a $J_{\mathrm{eff}} = 3/2$ quartet and $J_{\mathrm{eff}} = 1/2$ doublet. In IrO_6 octahedra, orbitals (p_x, p_y, and p_z) of six ligand oxygens (four basal or in-plane, and two apical) hybridize with these d orbitals. The modification of local structural parameters (Fig. 2) would change the hybridization with Pr substitution. For t_{2g}, while d_{xy} hybridizes only with basal p_x/p_y, the d_{xz} and d_{yz} participate with both basal p_z and apical p_x/p_y orbitals. In the case of the e_g state, the $d_{x^2-y^2}$ and d_{z^2} orbitals hybridize with p_x/p_y and p_z, respectively [35,37,38]. Figure 3(b) shows normalized O-K edge spectra for $x = 0.0$, 0.4, and 1.0 materials of the present series. As evident in the figure, two distinct peaks (marked by vertical dotted lines) in the low-energy regime are seen at binding energies (E_b) 528.95 and 532.77 eV, while a broad hump is observed between energies 534 and 548 eV. The energy gap between the first two peaks at the low-energy side is around 3.8 eV. In the low-energy side, the observed peak at 528.95 eV originates due to hybridization between Ir d_{xz}/d_{yz} and apical O p_x/p_y orbitals, while the peak at 532.77 eV arises due to bonding between Ir-t_{2g} with basal O-$2p$ orbitals. The broad hump at higher energy between 534 and 548 eV corresponds to the transition to hybridized states between the Ir e_g and O $2p$ orbitals. As seen in Fig. 3(b), the peak position at 528.95 eV does not show any significant change, but that at 532.77 eV shifts toward lower energy with the Pr amount. For the $x = 0.4$ and 1.0 material, we find that the peak at 532.77 eV changes by ~0.56 and 0.63 eV, respectively. The shifting of the second peak toward the low-energy side implies an increased hybridization of Ir-t_{2g} orbitals with basal O-$2p$ orbitals, which mostly arises due to the larger size of the Pr^{3+}ions. Here we note that the present analysis is based on the model of isolated t_{2g} and e_g orbitals. However, a recent theoretical calculation has shown the effect of CFE, SOC, and U on the mixing of t_{2g} and e_g orbitals, where the effect becomes prominent in the case of $5d$ transition metals [39]. While the low-energy peaks and high-energy hump in the XAS spectra are attributed to the hybridization of Ir-t_{2g}/O-p and Ir-e_g/O-p orbitals [Fig. 3(b) and above discussion], respectively, the positions of the peaks/hump are seen to vary across the composition and crystal structure [35,37,38,40]. Further, the O-K edge spectra in Fig. 3(b) show a prominent shoulder in the peaks/hump. Therefore, theoretical calculations are required to understand the possible role of t_{2g} and e_g orbital mixing on the XAS spectra of Ir-based materials.

We have also attempted to understand the valence state of Pr, which is important for its role in governing the electronic and magnetic properties. In Pr_6O_{11} (which is used as the ingredient for material synthesis), Pr exists in the mixed valence state of 3+ (Pr_2O_3) and 4+ (PrO_2). The measured M_4- and M_5-edge absorption spectra for the doped $x = 0.4$ and 1.0 samples of the present series are shown in Fig. 3(c). As evident in the figure, the line shape and peak position of the M_4 and M_5-edge absorption spectra are similar for both of these materials; however, the intensity of the $M_{4,5}$ increases with Pr concentration. The position of the M_5 and M_4 peaks is found to be around 930 and 949.3 eV, respectively, which closely matches with that for Pr^{3+} ions, while the corresponding peak positions for Pr^{4+} occur at higher energy [41,42]. This suggests that Pr is in the 3+ charge state, and thus shows an agreement with the Ir^{4+} charge state.

C. Magnetization study

Figure 4 shows the temperature (T)-dependent magnetization data (M) for the $(Y_{1-x}Pr_x)_2Ir_2O_7$ series where the data

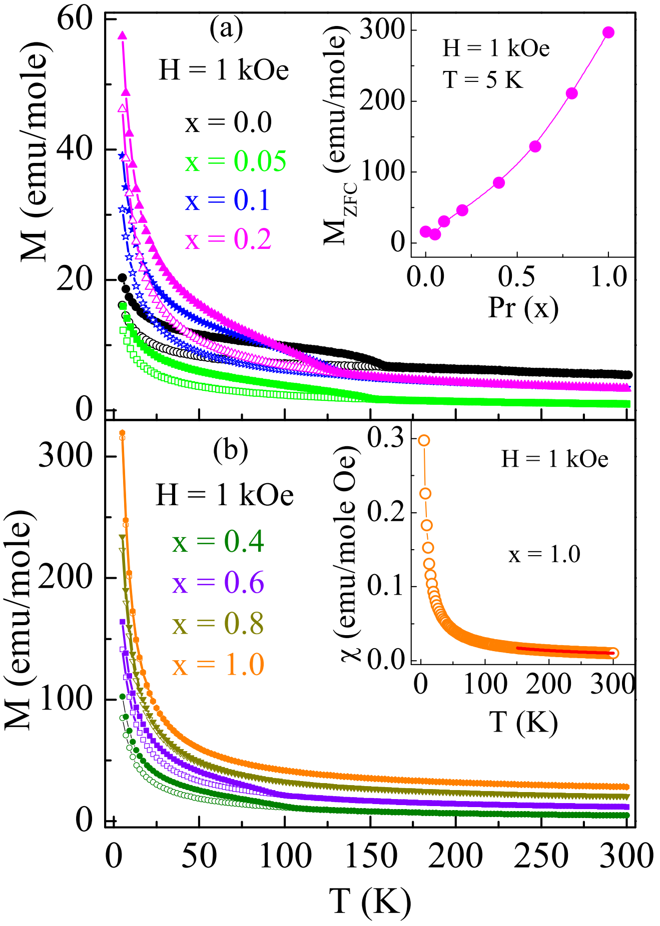

FIG. 4. Temperature-dependent magnetization data measured in 1 kOe under zero-field-cooled (ZFC) and field-cooled (FC) protocols for the $(Y_{1-x}Pr_x)_2Ir_2O_7$ series with (a) $x = 0.0$, 0.05, 0.1, 0.2, and (b) $x = 0.4$, 0.6, 0.8, 1.0 samples. The data in (b) are vertically shifted with 5, 12, and 18 emu/mole for $x = 0.6$, 0.8, 1.0. The inset of (a) shows the M_{ZFC} value at 5 K with the Pr level. The inset of (b) shows the magnetic susceptibility $\chi = M/H$ for $Pr_2Ir_2O_7$ ($x = 1.0$), where the solid line in the high-temperature regime is due to Eq. (1).

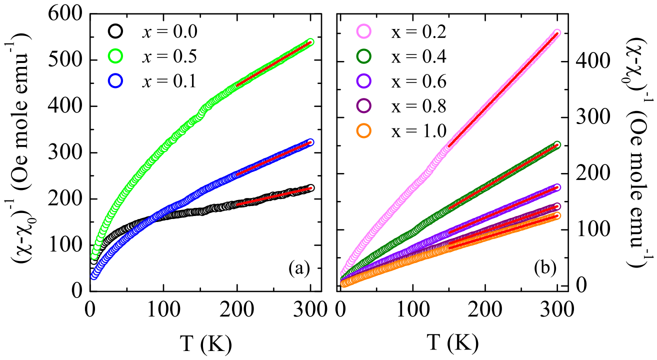

FIG. 5. Temperature-dependent inverse susceptibility $(\chi - \chi_0)^{-1}$ for the $(Y_{1-x}Pr_x)_2Ir_2O_7$ series with (a) $x = 0.0$. 0.05, 0.1, and (b) $x = 0.2$, 0.4, 0.6, 0.8, 1.0 compositions. The solid lines are due to straight-line fitting in the high-temperature regime.

have been collected following the zero-field-cooled (ZFC) and field-cooled (FC) protocol in an applied magnetic field of 1 kOe. It is evident in Fig. 4(a) that $M(T)$ for $Y_2Ir_2O_7$ exhibits a magnetic irreversibility between ZFC and FC magnetization around $T_N = 160$ K, opening a gap below this temperature [18,19]. This is considered to be an onset temperature for long-range AFM ordering. The M_{ZFC}, however, do not show any prominent cusp/peak around T_N. Here, it can be mentioned that the low-temperature magnetic state in $Y_2Ir_2O_7$ is quite intriguing as muon spin rotation (μSR) and neutron powder diffraction (NPD) experiments have shown an opposite result in the case of long-range magnetic ordering [12,13]. Recently, we have demonstrated that the low-temperature magnetic state in $Y_2Ir_2O_7$ as well as in its doped materials $Y_2(Ir_{1-x}M_x)_2O_7$ (M = Ru and Ti) has a nonequilibrium ground state [18–20]. The effect of Pr doping on magnetization is shown in Figs. 4(a) and 4(b). The notable observation is that except for $x = 0.05$, the magnetic moment at low temperature continuously increases with x [inset of Fig. 4(a)]. This increase of magnetic moment indicates a weakening of magnetic exchange interaction where the spins are unlocked from AFM interaction, hence yielding a higher moment. The transition temperature T_N, on the other hand, shows a continuous decrease with x, where for $Pr_2Ir_2O_7$ ($x = 1.0$), the M_{ZFC} and M_{FC} magnetizations merge completely, which implies a PM-like behavior [4].

For a high-temperature PM state, the magnetic susceptibility [$\chi = (M/H)$] has been analyzed using a modified Curie-Weiss law,

$$\chi = \chi_0 + \frac{C}{T - \theta_P}, \tag{1}$$

where χ_0, C, and θ_P are the temperature-independent magnetic susceptibility, the Curie constant, and the Curie-Weiss temperature, respectively. A representative fitting of $\chi(T)$ data with Eq. (1) in the temperature range between 150 and 300 K is shown in the inset of Fig. 4(b) as a solid line for $x = 1.0$. A reasonably good fitting with Eq. (1) implies that the magnetic state in a PM state obeys Curie-Weiss behavior. We obtain fitting parameters $\chi_0 = 2.3 \times 10^{-3}$ emu/mole, $C = 2.58(1)$, and $\theta_P = -22.8(4)$ K [4]. A similar good fitting has been obtained for the remaining samples in the present series. The corrected inverse susceptibility $(\chi - \chi_0)^{-1}$ vs T shows a linear behavior in the high-temperature regime (Fig. 5). Along with T_N, the composition-dependent θ_P are shown in Fig. 6(a). While T_N shows a linear decrease until $x = 0.8$, the $|\theta_P|$, on the other hand, shows a steep increase until $x = 0.2$, and then the changes are not significant. The obtained values of both T_N and $|\theta_P|$ for $x = 0.0$ and 1.0 materials agree with the reported values [4,18,19]. Here, it can be noted that for $Pr_2Ir_2O_7$, even though T_N vanishes, it exhibits a finite $|\theta_P|$. This finite $|\theta_P|$ arises due to Ir-5d electron-mediated AFM-type RKKY interactions among Pr-4f atoms [4]. Here, we caution that the magnetic parameters (θ_P, f, and μ_{eff}) in Fig. 6 are determined by fitting Eq. (1) in the temperature range from 150/200 K to 300 K. Though this temperature range is well within the PM state, it is indeed a limited temperature range, and one needs to check this fitting in an extended high-temperature range for a correct value. Nonetheless, the parameters are found

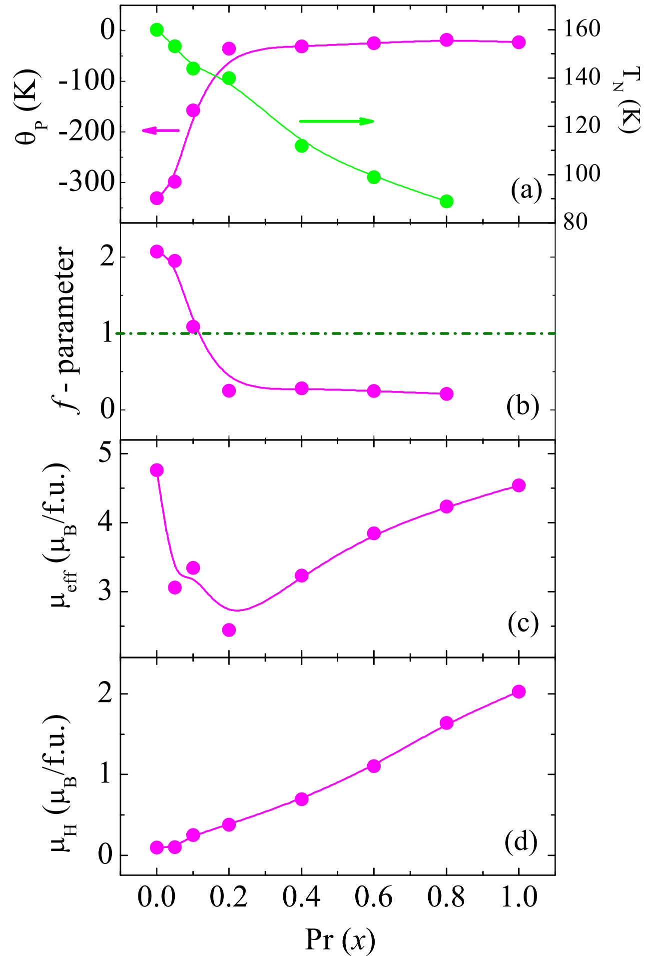

FIG. 6. (a) Curie-Weiss temperature θ_P and T_N, (b) frustration parameter f, (c) effective paramagnetic moment ($\mu_{\rm eff}$), and (d) moment μ_H at field 70 kOe with doping concentration x in the $(Y_{1-x}Pr_x)_2Ir_2O_7$ series. These parameters are obtained from the fitting of magnetization data with Eq. (1).

to be consistent with each other and agree with the previous reports.

The long-range magnetic ordering is, however, suppressed in $Pr_2Ir_2O_7$ due to the Kondo screening of Pr moments. We have further calculated the frustration parameter f ($|\theta_P|/T_N$) for the whole series, as shown in Fig. 6(b). This parameter provides vital information about a frustrated magnetic system where, for $f = 1$, the system realizes the magnetic ordering temperature according to its exchange-interaction strength. Here, it can be mentioned that the frustration parameter mainly applies to isotropic systems, and f much higher than 1 (usually > 10), for a system to be considered a frustrated system. In Fig. 6(b), the f parameter remains small for the present series; however, we have used this information to understand the evolution of the magnetic nature in the present series. The f value for $Y_2Ir_2O_7$ is calculated as 2.07, showing some level of frustration present in the system. For a low concentration of Pr, f decreases sharply and shows a value ~ 1 for $x = 0.1$. The $f < 1$ for $x > 0.1$ is quite intriguing as it indicates a low value of $|\theta_P|$ compared to its magnetic transition temperature T_N. This sudden suppression of $|\theta_P|$ occurs with the introduction of magnetic Pr^{3+} in the place of nonmagnetic Y^{3+}, where a further strengthening of exchange interaction would have been a possible scenario with x. This is quite surprising because a reasonably strong AFM-type exchange interaction and transition temperature ($T_N \sim 160$ K) in $Y_2Ir_2O_7$, which is mainly due to the Ir sublattice, is largely suppressed with an inclusion of magnetic Pr^{3+}, while the Ir sublattice remains unaltered. We believe that this weakening of $|\theta_P|$ is due to f-d interaction between localized Pr-4f and itinerant Ir-5d electrons. A RKKY-type f-d exchange-interaction-driven finite θ_P has been shown for $Pr_2Ir_2O_7$ [4]. The effect of f-d exchange interaction for pyrochlore iridates, in general, has been discussed in a recent study [11]. The f for $Pr_2Ir_2O_7$ could not be calculated due to the unavailability of T_N, but it has been reported to be ~ 170, implying it is a highly frustrated spin-liquid material [4]. Nonetheless, our results conclusively show a disappearance of the magnetic state with doping in the $(Y_{1-x}Pr_x)_2Ir_2O_7$ series, where the observed behavior has the similarity of a quantum phase transition (QPT). The prominent example of a doping-induced QPT is $Sr_{1-x}Ca_xRuO_3$, where the system shows vanishing of the magnetic state around 70% of Ca doping [43]. In the present series, the magnetic state disappears at more than 80% of Pr substitution. This calls for a detailed theoretical and experimental investigation as the quantum criticality has already been hinted at by the calculation for this series [27].

An effective PM moment ($\mu_{\rm eff}$) has been calculated from the obtained Curie constant C. As evident in Fig. 6(c), $\mu_{\rm eff}$ initially decreases and then increases, showing a dip around $x = 0.2$. The spin-only $\mu_{\rm eff} = g\sqrt{S(S+1)}\mu_B$, where $g = 2$ is the Landé g factor and $S = 1/2$, for $Y_2Ir_2O_7$ has been calculated with the value 3.46 μ_B/f.u. ($2Ir^{4+}$ ions per f.u.), which is lower than the experimentally obtained value 4.76 μ_B/f.u. [Fig. 6(c)]. For the doped materials, the $\mu_{\rm eff}$ can be calculated using $2\sqrt{[\mu_{\rm eff}^{Ir}]^2 + [(1-x)\mu_{\rm eff}^{Y}]^2 + x[\mu_{\rm eff}^{Pr}]^2}$. Given that $\mu_{\rm eff}^{Y}$ does not contribute and $\mu_{\rm eff}^{Pr} = 5.65$ μ_B/f.u., the expected $\mu_{\rm eff}$ for whole system will increase with x. However, the initial decrease of $\mu_{\rm eff}$ in the present series is probably due to the presence of local AFM-type Pr-Ir interaction in the PM state, which diminishes for $x > 0.2$. A lowering of the moment has also been observed in the $M(T)$ data in low-doped materials in Fig. 4(a).

Magnetic-field-dependent magnetization data $M(H)$ collected at 5 K are shown in Figs. 7(a) and 7(b) for the $(Y_{1-x}Pr_x)_2Ir_2O_7$ series. For $Y_2Ir_2O_7$, the $M(H)$ data are nonlinear with no sign of saturation until the highest measuring field of 70 kOe. With progressive substitution of Pr, major observations are that the nonlinearity in $M(H)$ increases and the magnetic moment μ_H at 70 kOe shows a continuous increase [Fig. 6(d)]. A close observation reveals that $M(H)$ for $Y_2Ir_2O_7$ show a small magnetic coercivity H_c ($\sim$100 Oe) and a remnant magnetization M_r ($\sim 4.7 \times 10^4$ μ_B/f.u.). The H_c almost vanishes with x. The $M(H)$ data are further plotted in the form of Arrott's plot [44] (M^2 vs H/M) for two end members, i.e., $x = 0.0$ and 1.0, respectively. A positive intercept due to straight-line fitting in Arrott's suggests a spontaneous magnetization or ferromagnetic (FM) behavior [19]. As seen

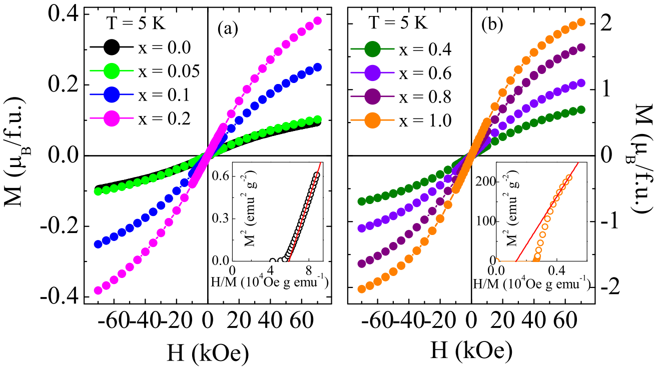

FIG. 7. Magnetic-field-dependent magnetization for the $(Y_{1-x}Pr_x)_2Ir_2O_7$ series with (a) $x = 0.0$, 0.05, 0.1, 0.2, and (b) $x = 0.4$, 0.6, 0.8, 1.0 compositions at 5 K. The insets of (a) and (b) show the Arrott plot of the $M(H)$ data for $x = 0.0$ and 1.0, respectively, where the solid lines are due to straight-line fitting.

in the insets of Fig. 7, both of the intercepts are negative, which is indicative of a non-FM state. As evident in the figure, the magnitude of the intercept decreases with Pr, which is in good agreement with the decrease of θ_P [Fig. 6(a)].

It can be mentioned here that similar hysteresis in the $M(H)$ data of $Y_2Ir_2O_7$ has previously been observed by Zhu *et al.* [16], who attribute it to the coexisting (weak) FM phase on top of the (large) AFM background. However, it would be difficult to reach a conclusion about the coexisting FM phase from such a small hysteresis loop alone. Further, such a weak FM phase is unlikely to be reflected in the Arrott plot.

D. Electrical transport

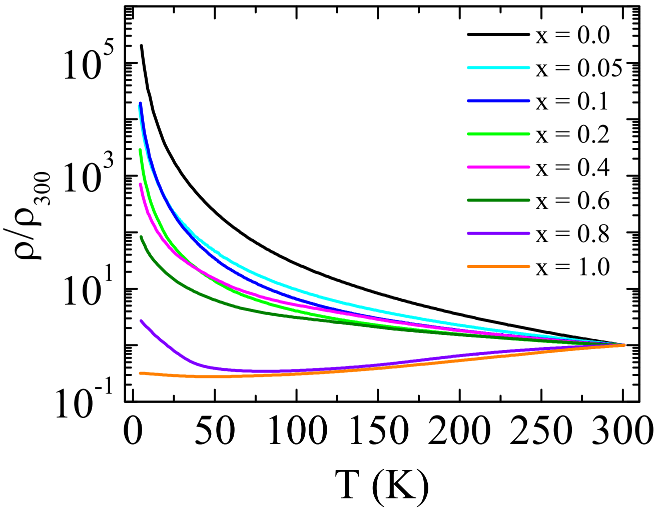

FIG. 8. Temperature-dependent resistivity normalized with ρ_{300} for the $(Y_{1-x}Pr_x)_2Ir_2O_7$ series.

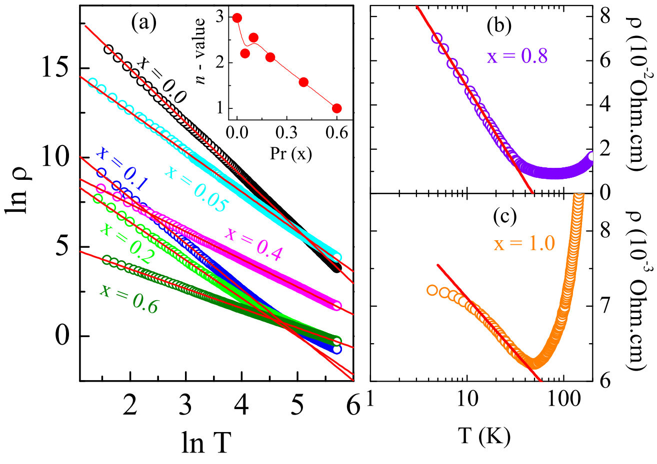

FIG. 9. (a) The $\rho(T)$ data are plotted in log-log scale for the $(Y_{1-x}Pr_x)_2Ir_2O_7$ series with $x = 0.0, 0.05, 0.1, 0.2, 0.4, 0.6$. The inset shows the composition-dependent exponent n [Eq. (2)], where the solid line is a guide to the eye. (b),(c) ρ vs $\ln T$ form for $x = 0.8$ and 1.0, respectively, where the solid lines are due to straight fittings.

The temperature-dependent resistivity $\rho(T)$ for the $(Y_{1-x}Pr_x)_2Ir_2O_7$ series is shown in Fig. 8 after normalizing with its value at 300 K, i.e., ρ_{300}. The $Y_2Ir_2O_7$ shows an insulating behavior where the resistivity increases by a couple of orders in going to low temperatures [12,18,19]. It is evident in the figure that ρ/ρ_{300} decreases continuously with substitution of Pr, while $Pr_2Ir_2O_7$ shows a metallic charge conduction [4]. In fact, resistivity at low temperature changes drastically by about 10 orders over the series. Along with a PM state, the arising of a metallic state in the robust AFM-insulating state of $Y_2Ir_2O_7$ with substitution of magnetic Pr^{3+} is quite intriguing. However, the other pyrochlore iridates $A_2Ir_2O_7$ with magnetic A-ion (i.e., Nd^{3+}, Sm^{3+}, Gd^{3+}) elements show a metal-insulator transition (MIT) with an insulating state at low temperature [10]. In addition to electron doping with its $4f^2$ structure, Pr^{3+} has comparatively higher ionic radii, which would induce local structural modifications that will influence the Ir-O hybridization. Indeed, an increased hybridization between Ir-t_{2g} and (basal) O-$2p$ orbitals has already been observed in Pr-doped materials [Fig. 3(b)]. This will facilitate the charge conduction, and hence a metallic state is expected. For $x = 0.8$, the $\rho(T)$ shows a MIT around 81 K, which closely matches with its magnetic transition temperature T_N [Fig. 6(a)]. Although $Pr_2Ir_2O_7$ $(x = 1.0)$ shows a metallic behavior, an upturn in its $\rho(T)$ is seen around 50 K, which is in agreement with a previous study [4]. The nature of electron conduction in insulating samples $(x \leqslant 0.6)$ has been analyzed with the following power-law behavior:

$$\rho = \rho_0 T^{-n}, \tag{2}$$

where n is an exponent. Figure 9(a) shows the $\rho(T)$ data in log-log scale where the straight lines are due to fitting of the data with Eq. (2). For $Y_2Ir_2O_7$, the exponent n has been obtained to be 2.98, which decreases with x [inset of Fig. 9(a)]. The semilogarithmic plotting of the $\rho(T)$ data for $x = 0.8$ and 1.0 materials shows a dip where a $\ln T$ dependence at low temperature implies a Kondo-like behavior [Figs. 9(b) and 9(c)].

A Kondo-like behavior has been indicated for $Pr_2Ir_2O_7$ $(x = 1)$ at low temperature [4]. For the compound with $x = 0.8$, there are two important observations: $\rho(T)$ follows a $\ln T$ dependence at low temperature [Fig. 9(b)] and the dip in $\rho(T)$ closely matches with its T_N (Fig. 8). Therefore, this dip in

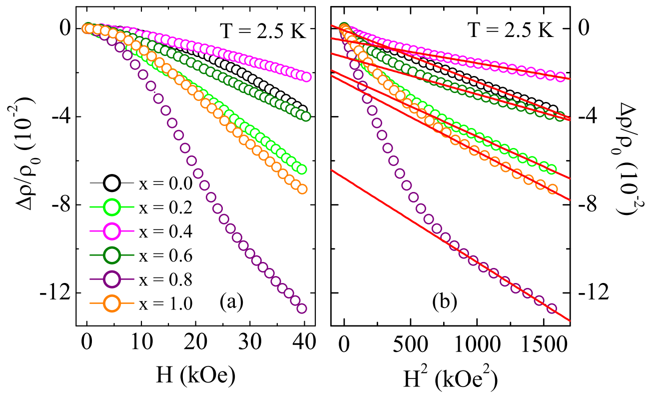

FIG. 10. (a) MR as a function of the magnetic field at 2.5 K for the $(Y_{1-x}Pr_x)_2Ir_2O_7$ series. (b) The same MR as the quadratic dependence of the magnetic field. The solid lines are due to straight-line fittings.

$\rho(T)$ may be either due to Kondo-like behavior as in $x = 1$ or a metal-insulator transition (MIT). This dip temperature (∼81 K) appears too high for Kondo behavior, in particular when the Pr site is diluted with nonmagnetic Y^{3+}. Here, the Kondo behavior arises due to f-d interaction between localized Pr-4f magnetic ions and itinerant Ir-5d electrons. Therefore, it would be unlikely that the Kondo temperature increases in going from $Pr_2Ir_2O_7$ to a 20%-diluted Pr lattice in $x = 0.8$. On the other hand, many pyrochlore iridates (i.e., $Nd_2Ir_2O_7$, $Sm_2Ir_2O_7$, and $Eu_2Ir_2O_7$) have shown a metal-insulator transition across its magnetic ordering temperature [10]. Given that dip temperature for $x = 0.8$ is reasonably high (∼81 K) and closely matches with its T_N, the low-temperature rise of $\rho(T)$ in this material is likely to be associated with the metal-insulator transition.

The calculated magnetoresistance (MR), $\Delta\rho/\rho(0) = [\rho(H) - \rho(0)]/\rho(0)$, for the $(Y_{1-x}Pr_x)_2Ir_2O_7$ series at 2.5 K is shown in Fig. 10(a). As evident in the figure, the MR is not very large, but their values are negative, i.e., conductivity increases in the presence of a magnetic field. Moreover, MR does not show a systematic variation with x, but the $x = 0.8$ material shows a highest MR. Usually, negative MR in such materials is largely due to the weak localization phenomenon, induced by the quantum interference effect. Recently, a quadratic field dependence of negative MR has been seen at low temperature for $Y_2Ir_2O_7$ [18]. Following that, MR data have been plotted as a function of H^2 in Fig. 10(b). As seen in Fig. 10(b), MR shows a H^2 dependence roughly above 25 kOe.

The insulating states in Ir-based pyrochlore materials are of general interest and have been investigated using different chemical substitutions at the Ir site, but very limited studies are reported regarding A-site doping. In the case of Pr^{3+} substitution in $(Nd_{1-x}Pr_x)_2Ir_2O_7$, the resistivity decreases and the MIT in the original system is suppressed for around 90% doping of Pr [45]. In the present case, the suppression of the insulating state with around 80% of Pr implies a similar result. A transition from an insulating to metallic state in pyrochlore iridates appears to be related to the ionic radii of the A-site cation [10]. Here, Pr^{3+} has larger ionic radii (1.126 Å) compared to Y^{3+} (1.019 Å), and therefore it would be likely to enhance the electronic conductivity by reducing the trigonal distortion of IrO_6 octahedra or, equivalently, increasing the Ir-O orbital hybridization [7,46]. For the present $x = 0.8$ sample (MIT temperature ∼81 K), we have calculated the average ionic radii to be 1.1054 Å, which almost matches with that of Nd^{3+} (1.109 Å). Here, note that $Nd_2Ir_2O_7$ exhibits a MIT around 33 K [10], and this small difference in MIT temperature with our $x = 0.8$ sample is due to a slight difference in the ionic radii.

The decrease of resistivity as well as MIT in the present $(Y_{1-x}Pr_x)_2Ir_2O_7$ series are quite likely due to an increase of the average A-site ionic radii. It can be noted that similar suppression of the insulating state has previously been observed in $Y_2Ir_2O_7$ with Ca and Bi substitution at the Y site [15–17,47]. The Ca^{2+} (1.12 Å) acts for hole doping in $Y_2Ir_2O_7$, and the complete suppression of insulating behavior occurs around 15% of Ca doping [15,16]. Similarly, $Bi_2Ir_2O_7$ shows complete metallic behavior, where Bi^{3+} (1.17 Å) has slightly higher ionic radii compared to Pr^{3+} [48]. A complete suppression of both the insulating and magnetic state occurs around 50% of Bi doping in $Y_2Ir_2O_7$ at the Y site [47]. The calculated average ionic radii of a 50% Bi-doped sample is 1.097 Å, which is close to the value of our present 80% Pr-doped sample. Furthermore, it was previously observed that both MIT and the magnetic phase for $Eu_2Ir_2O_7$ are suppressed with 10% of Bi doping at the Eu site; however, the average ionic size is found to be 1.076 Å [49]. Moreover, it is observed that the MIT across the T_N in pyrochlore iridates occurs for materials which have an average ionic size of A-site cations between 1.066 and 1.109 Å [10]. Therefore, the observed minimum in $\rho(T)$ for $x = 0.8$ is likely a MIT driven by magnetic ordering temperature. The prominent effect of A-site ionic radii on local structural parameters (trigonal distortion and Ir-O bond length/angle) in Fig. 2 indicates an increasing overlap between Ir-d and O-2p orbitals with Pr doping, which has, indeed, been observed in spectroscopy measurements in Fig. 3. While the metal-insulating state in pyrochlore iridates is being seriously investigated, our results will hopefully shed light in this direction. However, in addition to orbital hybridization, any possible role of the f-d interaction on electronic transport needs to be understood using theoretical calculations.

IV. CONCLUSION

In summary, detailed structural, magnetic, and transport properties are studied in a series of polycrystalline samples, $(Y_{1-x}Pr_x)_2Ir_2O_7$, with $x \leqslant 1.0$. Structural analysis shows that the system retains its original $Fd\bar{3}m$ cubic symmetry, while the structural parameters show systematic changes with Pr. In particular, the distortion of IrO_6 octahedra decreases with x. The doped Pr increases overlapping/hybridization between Ir-t_{2g} and basal O-p orbitals, as evident from the XAS data. Magnetization measurements reveal that the magnetic state is weakened with Pr substitution, where $Pr_2Ir_2O_7$ shows complete paramagnetic behavior. The parent compound $Y_2Ir_2O_7$ is a strong insulator, but the Pr substitution decreases the electrical resistivity in the whole series. For $x = 0.8$, a metal-insulator transition is observed around 81 K, while the end member of this series, $Pr_2Ir_2O_7$, shows metallic behavior in the whole temperature range. The nature of charge conduction is found to follow the power-law behavior for $x \leqslant 0.6$, while a Kondo-like behavior is observed at low temperature for $(Y_{0.2}Pr_{0.8})_2Ir_2O_7$ and $Pr_2Ir_2O_7$ materials. A whole series of samples exhibits a weak negative MR at low temperature, which shows quadratic field dependence at higher field.

ACKNOWLEDGMENTS

We acknowledge UGC-DAE CSR, Indore for the magnetic measurements. We are thankful to DST-FIST and DSR-PURSE for supporting the 'low-temperature high-magnetic-field' and 'helium liquefier' facility and for the other financial supports. H.K. acknowledges UGC, India for the financial support of a BSR fellowship. The authors thank Prof. J-F. Lee, Prof. J-M. Chen, and Prof. Shu-Chih Haw for their support in the XAS measurements.

[1] M. J. P. Gingras, C. V. Stager, N. P. Raju, B. D. Gaulin, and J. E. Greedan, Phys. Rev. Lett. **78**, 947 (1997).
[2] S. Yoshii and M. Sato, J. Phys. Soc. Jpn. **68**, 3034 (1999).
[3] J. S. Gardner, S. R. Dunsiger, B. D. Gaulin, M. J. P. Gingras, J. E. Greedan, R. F. Kiefl, M. D. Lumsden, W. A. MacFarlane, N. P. Raju, J. E. Sonier, I. Swainson, and Z. Tun, Phys. Rev. Lett. **82**, 1012 (1999).
[4] S. Nakatsuji, Y. Machida, Y. Maeno, T. Tayama, T. Sakakibara, J. van Duijn, L. Balicas, J. N. Millican, R. T. Macaluso, and J. Y. Chan, Phys. Rev. Lett. **96**, 087204 (2006).
[5] S. T. Bramwell, M. J. Harris, B. C. den Hertog, M. J. P. Gingras, J. S. Gardner, D. F. McMorrow, A. R. Wildes, A. L. Cornelius, J. D. M. Champion, R. G. Melko, and T. Fennell, Phys. Rev. Lett. **87**, 047205 (2001).
[6] H. Fukazawa, R. G. Melko, R. Higashinaka, Y. Maeno, and M. J. P. Gingras, Phys. Rev. B **65**, 054410 (2002).
[7] W. Witczak-Krempa, G. Chen, Y. B. Kim, and L. Balents, Ann. Rev. Condens. Matter Phys. **5**, 57 (2014).
[8] J. S. Gardner. M. J. P. Gingras, and J. E. Greedan, Rev. Mod. Phys. **82**, 53 (2010).
[9] D. Pesin and L. Balents, Nat. Phys. **6**, 376 (2010).
[10] K. Matsuhira, M. Wakeshima, Y. Hinatsu, and S. Takagi, J. Phys. Soc. Jpn. **80**, 094701 (2011).
[11] G. Chen and M. Hermele, Phys. Rev. B **86**, 235129 (2012).
[12] S. M. Disseler, C. Dhital, A. Amato, S. R. Giblin, C. de la Cruz, S. D. Wilson, and M. J. Graf, Phys. Rev. B **86**, 014428 (2012).
[13] M. C. Shapiro, S. C. Riggs, M. B. Stone, C. R. de la Cruz, S. Chi, A. A. Podlesnyak, and I. R. Fisher, Phys. Rev. B **85**, 214434 (2012).
[14] N. Taira, M. Wakeshima, and Y. Hinatsu, J. Phys.: Condens. Matter **13**, 5527 (2001).
[15] H. Fukazawa and Y. Maeno, J. Phys. Soc. Jpn. **71**, 2578 (2002).
[16] W. K. Zhu, M. Wang, B. Seradjeh, F. Yang, and S. X. Zhang, Phys. Rev. B **90**, 054419 (2014).
[17] M. Soda, N. Aito, Y. Kurahashi, Y. Kobayashi, and M. Sato, Physica B **329-333**, 1071 (2003).
[18] H. Kumar and A. K. Pramanik, J. Magn. Magn. Mater **409**, 20 (2016).
[19] H. Kumar, R. S. Dhaka, and A. K. Pramanik, Phys. Rev. B **95**, 054415 (2017).
[20] H. Kumar and A. K. Pramanik, J. Phys. Chem. C **123**, 13036 (2019).
[21] H. Kumar and A. K. Pramanik, J. Magn. Magn. Mater. **478**, 148 (2019).
[22] V. K. Dwivedi and S. Mukhopadhyay, J. Appl. Phys. **126**, 165112 (2019).
[23] S. M. Disseler, Phys. Rev. B **89**, 140413(R) (2014).
[24] X. Wan, A. M. Turner, A. Vishwanath, and S. Y. Savrasov, Phys. Rev. B **83**, 205101 (2011).
[25] Y. Tokiwa, J. J. Ishikawa, S. Nakatsuji, and P. Gegenwart, Nat. Mater. **13**, 356 (2014).
[26] Y. Machida, S. Nakatsuji, Y. Maeno, T. Tayama, T. Sakakibara, and S. Onoda, Phys. Rev. Lett. **98**, 057203 (2007).
[27] L. Savary, E.-G. Moon, and L. Balents, Phys. Rev. X **4**, 041027 (2014).
[28] J. Rodríguez-Carvajal, Phys. B **192**, 55 (1993).
[29] K. Kimura, Y. Ohta, and S. Nakatsuji, J. Phys.: Conf. Ser. **400**, 032040 (2012).
[30] J. N. Millican, R. T. Macaluso, S. Nakatsuji Y. Machida, Y. Maeno, and J. Y. Chan, Mater. Res. Bull. **42**, 928 (2007).
[31] J. P. Clancy, H. Gretarsson, E. K. H. Lee, D. Tian, J. Kim, M. H. Upton, D. Casa, T. Gog, Z. Islam, B.-G. Jeon, K. H. Kim, S. Desgreniers, Y. B. Kim, S. J. Julian, and Y.-J. Kim, Phys. Rev. B **94**, 024408 (2016).
[32] L. Hozoi, H. Gretarsson, J. P. Clancy, B.-G. Jeon, B. Lee, K. H. Kim, V. Yushankhai, P. Fulde, D. Casa, T. Gog, J. Kim, A. H. Said, M. H. Upton, Young-June Kim, and J. van den Brink, Phys. Rev. B **89**, 115111 (2014).
[33] B. J. Kim, H. Ohsumi, T. Komesu, S. Sakai, T. Morita, H. Takagi, and T. Arima, Science **323**, 1329 (2009).
[34] J. P. Clancy, N. Chen, C. Y. Kim, W. F. Chen, K. W. Plumb, B. C. Jeon, T. W. Noh, and Y.-J. Kim, Phys. Rev. B **86**, 195131 (2012).
[35] X. Liu, Y. Cao, B. Pal, S. Middey, M. Kareev, Y. Choi, P. Shafer, D. Haskel, E. Arenholz, and J. Chakhalian, Phys. Rev. Mater. **1**, 075004 (2017).
[36] M. A. Laguna-Marco, P. Kayser, J. A. Alonso, M. J. Martinez-Lope, M. van Veenendaal, Y. Choi, and D. Haskel, Phys. Rev. B **91**, 214433 (2015).
[37] S. Seong, D. H. Kim, E. Lee, A. Biswas, Y. H. Jeong, B. I. Min, B. Kim, Y. Kim, J. Baik, and J.-S. Kang, J. Appl. Phys. **124**, 205102 (2018).
[38] V. Ilakovac, A. Louat, A. Nicolaou, J.-P. Rueff, Y. Joly, and V. Brouet, Phys. Rev. B **99**, 035149 (2019).
[39] G. L. Stamokostas and G. A. Fiete, Phys. Rev. B **97**, 085150 (2018).
[40] C. H. Sohn, D.-Y. Cho, C.-T. Kuo, L. J. Sandilands, T. F. Qi, G. Cao, and T. W. Noh, Sci. Rep. **6**, 23856 (2016).
[41] J. Herrero-Martin, J. L. Garcia-Munoz, S. Valencia, C. Frontera, J. Blasco, A. J. Baron-Gonzalez, G. Subias, R. Abrudan, F. Radu, E. Dudzik, and R. Feyerherm, Phys. Rev. B **84**, 115131 (2011).

[42] Z. Hu, G. Kaindl, H. Ogasawara, A. Kotani, and I. Felner, Chem. Phys. Lett. **325**, 241 (2000).

[43] D. Fuchs, M. Wissinger, J. Schmalian, C.-L. Huang, R. Fromknecht, R. Schneider, and H. v. Löhneysen, Phys. Rev. B **89**, 174405 (2014)

[44] A. Arrott, Phys. Rev. **108**, 1394 (1957).

[45] K. Matsuhira, K. Kuroda, T. Sakakibara, M. Wakeshima, and Y. Hinatsu, JPS Conf. Proc. **3**, 013017 (2014).

[46] B.-J. Yang and Y. B. Kim, Phys. Rev. B **82**, 085111 (2010).

[47] N. Aito, M. Soda, Y. Kobayashi, and M. Sato, J. Phys. Soc. Jpn. **72**, 1226 (2003).

[48] T. Qi, O. Korneta, X. Wan, L. DeLong, P. Schlottmann, and G. Cao, J. Phys.: Condens. Matter **24**, 345601 (2012).

[49] P. Telang, K. Mishra, G. Prando, A. K. Sood, and S. Singh, Phys. Rev. B **99**, 201112(R) (2019).